Energy Proceedings
Vol 36, 2023
ISSN 2004-2965

Solar CO_2 splitting coupling with PV, photon-enhanced thermionic emission cell and SOEC for efficient full-spectrum utilization in a wide temperature range

Hongsheng Wang[1], Tong Liu[2], Hui Kong [2*]

1 School of Energy and Environment, City University of Hong Kong, Kowloon, Hong Kong SAR, China

2 School of Mechanical Engineering, Beijing Institute of Technology, Beijing 100081, China.
(* Corresponding Author: konghui2020@bit.edu.cn)

ABSTRACT

CO_2 splitting driven by solar energy is a clean and promising approach for addressing the issue of CO_2 emission and approaching the dual-carbon target. Here, a high-efficient solar CO_2 electrolysis system containing photovoltaic (PV) cell, photon-enhanced thermionic emission cell (PETE), and solid oxide electrolysis cell (SOEC) is proposed. CO_2 serves as cool fluid to decrease the temperature of PV cells for the enhancement of PV efficiency, and the heated CO_2 by PV cells and PETE is fed into SOEC at a high temperature to decrease the Gibbs free energy utilized in electrolysis. The combination of PV cell and PETE can enlarge the temperature range for full solar spectrum utilization. Compared to H_2O splitting in SOEC, CO_2 splitting can convert more thermal energy with relatively low energy level into high-energy-level chemical energy. The system can reach the energy efficiency, exergy efficiency, and solar-to-fuel efficiency of 73.5%, 48.0%, and 33.3%, respectively. This research sheds light on high-efficient solar CO_2 splitting system design with full solar spectrum utilization in a wide temperature range.

Keywords: solar CO_2 splitting, full solar spectrum utilization, photon-enhanced thermionic emission cell (PETE), solid oxide electrolysis cell (SOEC), photovoltaic/thermal (PVT) collector, Gibbs free energy

NONMENCLATURE

Abbreviations	
PETE	photon-enhanced thermionic emission cell
PV	photovoltaic
SOEC	solid oxide electrolysis cell
Symbols	
A	the area of the photovoltaic/PETE module to receive solar energy, m^2
A_{PV}	surface area of PV cell, m^2
B_g	flow permeability, m^2 (darcy)
C	concentration ratio, -
C_{p,T_i,CO_2}	the specific heat of CO_2 at T_i, J mol^{-1} K^{-1})
$D^{eff}_{CO_2}$	the effective diffusion coefficient of CO_2, m^2 s^{-1}
d_a	the thickness of anode, m
d_c	the thickness of cathode, m
E	reversible potential, V
$E_{act,a}$	anode activation energy, J mol^{-1}
$E_{act,c}$	cathode activation energy, J mol^{-1}
E_{tot}	total solar radiant energy before concentrating, J
E_{abs}	the absorbed energy, J
Ex_{CO}	exergy of CO, J mol^{-1}
$\dot{E}x_{solar}$	exergy input rate of solar energy, J
F	Faraday constant, C mol^{-1}
$\triangle G$	Gibbs free energy change, J mol^{-1}
h	convective heat transfer coefficient, W m^{-2} K^{-1})
H	height of the heating section, m
HHV_{CO}	higher heating value of CO, J mol^{-1}
$\triangle H$	enthalpy change, J mol^{-1}
I	irradiation intensity, W m^{-2}
J	current density, A m^{-2}
$J_{0,a}$	exchange current densities of the anode, A m^{-2}
$J_{0,c}$	exchange current densities of the cathode, A m^{-2}
L	length of the heating section, m
L_e	thickness of the electrolyte, m
L_{PV}	length of PV cell, m
$l_{electrolyte}$	electrolyte thickness, m
l_{anode}	anode thickness, m
$l_{cathode}$	cathode thickness, m
$\dot{n}_{CO}$	flow rate of CO generated, mol s^{-1}
$\dot{Q}_{diss}$	thermal power from PV and PETE module, W

This is a paper for the 9th Applied Energy Symposium: Low Carbon Cities and Urban Energy Systems (CUE2023), Sep. 2-7, 2023, Matsue & Tokyo, Japan.

$\dot{Q}_{\mathrm{rad,loss}}$	rate of radiative heat loss, W
$\dot{Q}_{\mathrm{conv,loss}}$	rate of convective heat loss, W
$\dot{Q}_{\mathrm{CO_2,\,ab}}$	thermal power absorbed by CO_2 in each control volume, W
$\dot{Q}_{\mathrm{CO_2}}$	thermal power of CO_2 output from the SOEC electrolyzer, W
R	universal gas constant, J mol^{-1} K^{-1})
$\triangle S$	entropy change, J mol^{-1} K^{-1}
T	temperature, K
T_0	ambient temperature, K
T_{sun}	temperature of the sun surface, K
T_{sky}	sky temperature, K
$\triangle T$	temperature difference between photovoltaic panel and CO_2 flow, K
V	electric potential, V
W	width of the heating section, m
W_{PV}	electricity generated from PV cell, J
W_{PETE}	electricity generated from PV cell, J
W_{tot}	total electricity generated from solar energy in both PV and PETE module, J
$\dot{W}_{\mathrm{tot}}$	total electricity power generated from PV module and PETE module, W
z	the number of electrons produced per reaction, -
Greek Symbols	
α	symmetry factor or the charge transfer coefficient, -
γ_{a}	pre-exponential factors of the anode, A m^{-2}
γ_{c}	pre-exponential factors of the cathode, A m^{-2}
ε	photovoltaic module emissivity, -
χ	electron affinity on the cathode surface, eV
$\eta_{\mathrm{act,a}}$	activation overpotential of the anode, V
$\eta_{\mathrm{act,c}}$	activation overpotential of the cathode, V
$\eta_{\mathrm{con,a}}$	concentration overpotential of anode, V
$\eta_{\mathrm{con,c}}$	concentration overpotential of cathode, V
η_{en}	first-law thermodynamic efficiency (solar energy efficiency), -
η_{ex}	second-law thermodynamic efficiency (exergy efficiency), -
η_{mod}	module efficiency, -
η_{ohmic}	ohmic overpotential, V
η_{opt}	optical efficiency, -
$\eta_{T_i,\mathrm{PV}}$	efficiency of PV cell at the temperature of T_i , -
$\eta_{T_i,\mathrm{PETE}}$	efficiency of PETE module at the temperature of T_i, -
$\eta_{T_i,\mathrm{cell}}$	efficiency of the multi-junction GaAs PV cell, -

1. INTRODUCTION

Carbon dioxide (CO_2) capture, conversion, and utilization is significant for addressing the issue of global warming induced by greenhouse emission [1]. Solar CO_2 splitting for CO generation and other hydrocarbons downstream (e.g., by Fischer-Tropsch synthesis) is a clean and sustainable approach, which can not only convert CO_2 into energy carrier and chemical feedstock, but also store the discontinuous and low-energy-density solar irradiation as chemical energy for convenient storage and utilization [2, 3]. Several promising methods have been proposed, e.g., chemical cycle [4], membrane reactor [5], but they are still limited by the low efficiency (e.g., c.a. 5% in experiments [5]).

CO_2 splitting in solid oxide electrolysis cell (SOEC) is a high-efficient way driven by electricity with a high energy level, and it is also regarded as a promising approach for solar power storage via photovoltaic (PV) cells [6]. Separated application of solar power generation via PV cells and CO_2 electrolysis in SOEC have some shortages: 1) only a certain range of solar spectrum can be absorbed by PV cells, and efficiency of solar energy utilization is low; 2) the unabsorbed solar energy will be converted into heat to increase the temperature of PV cells, resulting in a low PV efficiency; 3) traditional CO_2 electrolysis in SOEC is totally driven by electricity, which has a high energy level, and it can be further optimized for rational arrangement of energy species. Though PV/thermal (PVT) collector has been proposed to utilized the full spectrum of solar energy and increase the PV efficiency [7], the working temperature between PV cells and SOEC still has a huge gap that the upper limit of PV cell temperature and typical operating temperature of SOEC are 250 °C and 800 °C, and thus other heating processes (typically heating by electricity) are still required.

To address the issues above, a system consists of PV cells, photon-enhanced thermionic emission cell (PETE), and SOEC for solar CO_2 splitting is proposed in this research. The CO_2 at room temperature serves as cooling fluid for PV cells to enhance the PV efficiency, and CO_2 are heated by PV cells (< 250 °C) and PETE (250 °C to reaction temperature of SOEC, e.g., 800 °C) sequentially for reaching the temperature of SOEC operation. With the assistance of PV cells and PETE, the temperature of electrolysis increases, which can decrease the requirement of Gibbs free energy (electricity) requirement, exhibited in Figure 1, leading to a win-win result: power generated by PV cells increases and

electricity required in SOEC decreases. Compared to solar water splitting, CO_2 splitting can convert more ratio of thermal energy ($T\Delta S/\Delta H$, numerically given in Figure 1c) with low energy level into high-energy-level chemical energy at high temperatures (> 100 °C), facilitating solar thermal energy conversion and storage.

To the best of our knowledge, this is the first time to utilize full solar spectrum for solar CO_2 splitting covering a wide temperature range from room temperature to the temperature of SOEC operation, which has unique advantages in thermodynamics as described above, giving guidance for rational design of high-efficient solar CO_2 splitting systems.

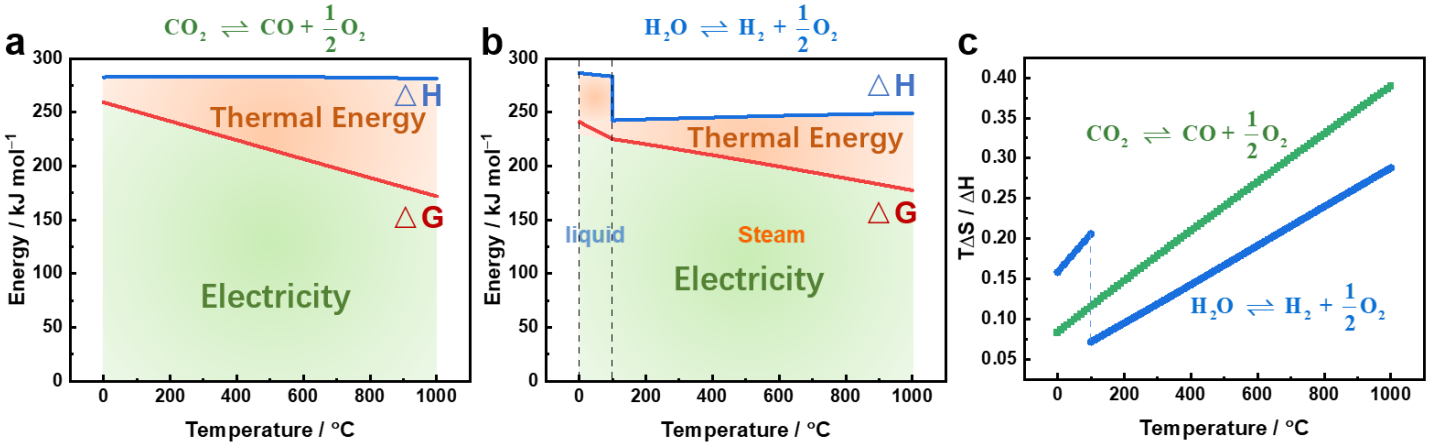

Figure 1. Thermodynamic data of (a) CO_2 and (b) H_2O electrolysis under one atmosphere and (c) the comparison of thermal energy required for electrolysis of CO_2 and H_2O. Electrolysis of CO_2 can convert higher ratio of thermal energy with relatively low energy level into high-energy-level chemical energy compared to the electrolysis of H_2O at the temperature > 100 *°C*.

2. MATHEMATICAL MODEL

2.1 Introduction of the proposed system

The proposed system can convert CO_2 into CO driven by full-spectrum solar energy efficiently. As the illustration in Figure 2a, b, the CO_2 at room temperature is first heated by PV cells and PETE, where CO_2 can be heated to a high temperature utilizing the recycled thermal energy released by PV and PETE, and then the heated CO_2 can be split into CO in SOEC. The total reaction is:

$$CO_2 \rightleftharpoons CO + \frac{1}{2}O_2 \qquad (1)$$

The total energy required in the splitting reaction is ΔH (Figure 1a, b), which equals to the sum of Gibbs free energy (ΔG, electricity) and ($T\Delta S$, thermal energy):

$$\Delta H = \Delta G + T\Delta S \qquad (2)$$

The electrode reactions in SOEC (Figure 2c) are shown below:

$$CO_2 + 2e^- \rightarrow CO + O^{2-}(\text{cathode}) \qquad (3)$$

$$O^{2-} \rightarrow 2e^- + \frac{1}{2}O_2(\text{anode}) \qquad (4)$$

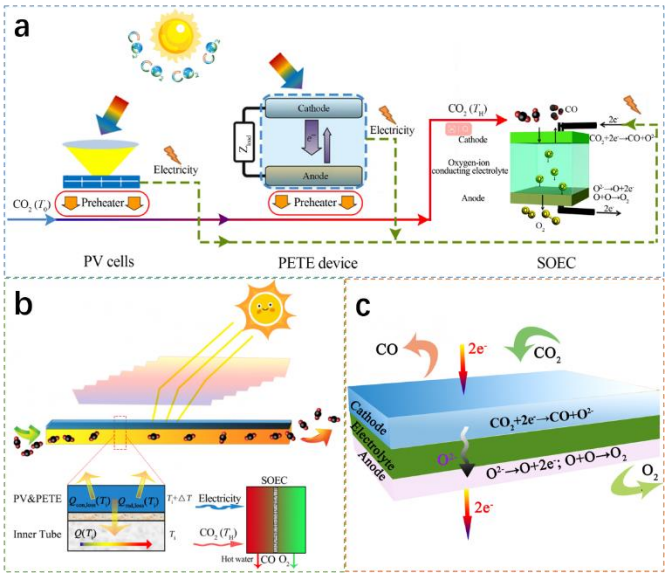

Figure 2. Illustration of the solar CO_2 splitting system. (a) Schematic chart for the material flow and energy flow; (b) Schematic diagram of the heat transfer process; (c) Schematic diagram of CO generation with oxygen ion separation in SOEC.

2.2 Mathematical Model for heating process

In this section, mass and energy balances are considered in each control volume (heat losses of convection and radiation are shown in Figure 2b), and the momentum balance is neglected due to its weak impact on the performance [8]. In the flow channel, it has been divided into multiple micro-elements along the length direction, and the corresponding temperature of the CO_2 flow inside is T_i.

The solar irradiation is first concentrated by a line-focused concentrator. Because of the optical loss during concentrating, only part of the solar energy is absorbed by the system, and the absorbed energy can be expressed as:

$$\delta E_{\mathrm{abs}}(T_i) = \delta E_{\mathrm{tot}} \cdot \eta_{\mathrm{opt}} \tag{5}$$

where E_{tot} is the total solar radiant energy before concentrating, which equals to $I \times A \times t$ (the product of direct normal irradiation, area for receiving solar energy, and irradiation time), and η_{opt} is the optical efficiency, which listed in Table 1 along with other key parameters in this simulation. Part of the absorbed energy is converted into electrical energy through the PV cell or PETE, and electricity generated can be expressed as:

$$\delta W_{\mathrm{PV}}(T_i) = \delta E_{\mathrm{abs}}(T_i) \cdot \eta_{T_i,\mathrm{PV}} \tag{6}$$

$$\delta W_{\mathrm{PETE}}(T_i) = \delta E_{\mathrm{abs}}(T_i) \cdot \eta_{T_i,\mathrm{PETE}} \tag{7}$$

where $\eta_{T_i,\mathrm{PV}}$ and $\eta_{T_i,\mathrm{PETE}}$ are the solar-to-electric efficiency of the PV cell and PETE module at the temperature of T_i, respectively; W_{PV} and W_{PETE} are the electricity generated from PV cell and PETE module, respectively.

Multi-junction GaAs PV cells are utilized as the electricity generation device below 250 °C, and the efficiency of the entire PV module is exhibited as below [9]:

$$\eta_{T_i,\mathrm{PV}} = \eta_{T_i,\mathrm{cell}} \cdot \eta_{\mathrm{mod}} \tag{8}$$

where $\eta_{T_i,\mathrm{cell}}$ is the efficiency of the multi-junction GaAs PV cell; η_{mod} is module efficiency defined as the ratio of the efficiency of PV module to that of the PV cell. When the temperature is T_i, the multi-junction GaAs PV cell efficiency is expressed below [9]:

$$\eta_{T_{i,\mathrm{cell}}} = \eta_{T_{i,0}} + 0.0142 \ln C + (-0.000715 + 6.97 \times 10^{-5} \ln C) \times (T_i + \Delta T - T_0),\ C \leqslant 200 \tag{9}$$

where C is the concentration ratio, and ΔT is the temperature difference between the photovoltaic module and the CO_2 flow, given as 10 °C in this study. The values of $\eta_{T_{i,0}}$ are 29.8% [9] and 37.2% [10] for triple-junction and quadruple-junction GaAs PV cell at 25 °C, respectively. The quadruple-junction GaAs PV cell has a higher efficiency than that of triple-junction GaAs PV cell due to a wider band gap with a high cost. In this research, the triple-junction GaAs PV cell is utilized for simulation, and the efficiency of quadruple-junction GaAs PV cell is given in Figure 3b for comparison.

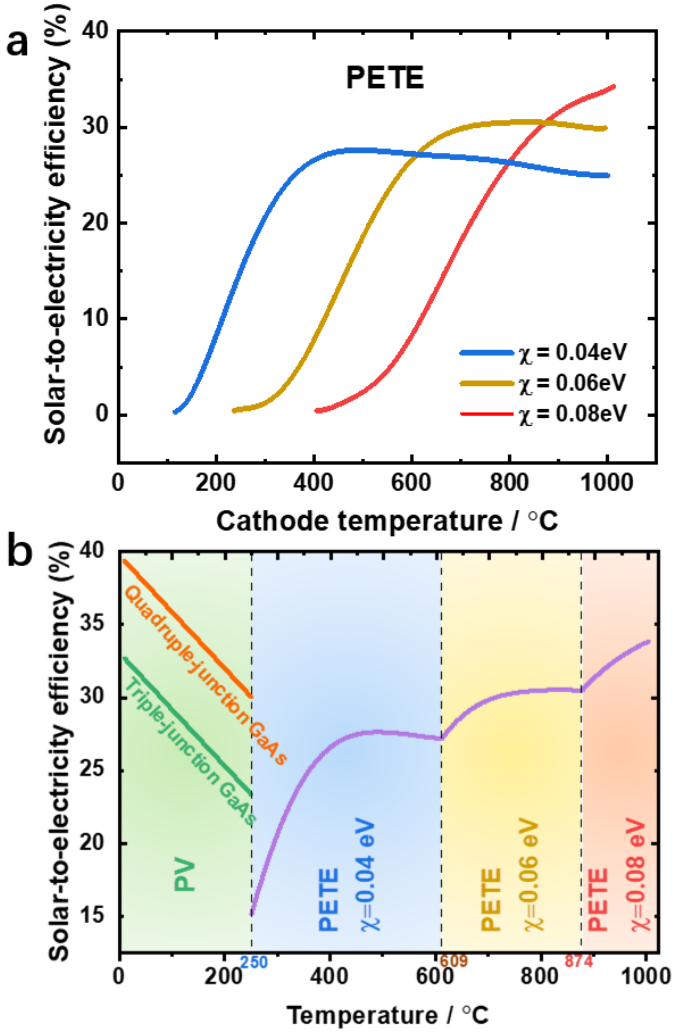

Figure 3. (a) The solar-to-electricity efficiency of PETE materials with different affinities to the cathode temperature. (b) The solar-to-electricity efficiency of triple-junction, quadruple-junction GaAs and PETE as a function of temperature for the proposed system with the concentration ratio C of 60.

PETE modules are used as the power generation devices at above 250 °C. The power generation efficiency of PETE modules is varied with the temperature and the electron affinity on the cathode surface (χ), which is shown in Figure 3(a), and the higher values of solar-to-electricity efficiency of the PETE modules with different χ are selected in this research (Figure 3(b)). The equations of solar-to-electricity efficiency of PETE with

different χ in this research are given as below [11]:

$$\eta_{T_i,\mathrm{PETE}} = 0.41163 - 9.3412\times10^{-3}T + 7.3927\times10^{-5}T^2 - 2.5151\times10^{-7}T^3 + 4.5432\times10^{-10}T^4 - 4.5639\times10^{-13}T^5 + 2.4116\times10^{-16}T^6 - 5.2328\times10^{-20}T^7,\ \chi = 0.4\mathrm{eV}$$

$$\eta_{T_i,\mathrm{PETE}} = -2.38144 + 3.7360\times10^{-2}T - 2.34382\times10^{-4}T^2 + 7.561\times10^{-7}T^3 - 1.35138\times10^{-9}T^4 + 1.36022\times10^{-12}T^5 - 7.2428\times10^{-16}T^6 + 1.59043\times10^{-19}T^7,\ \chi = 0.6\mathrm{eV}$$

$$\eta_{T_i,\mathrm{PETE}} = -9.4176 + 8.8734\times10^{-2}T - 3.3662\times10^{-4}T^2 + 6.5628\times10^{-7}T^3 - 6.9475\times10^{-10}T^4 + 3.8473\times10^{-13}T^5 - 9.1502\times10^{-17}T^6 + 2.8839\times10^{-21}T^7,\ \chi = 0.8\mathrm{eV} \quad (10)$$

In addition to being used for electricity generation, part of the residual solar energy is taken away by the CO_2 flow, and another part of the residual heat is wasted by the convection and radiation losses (illustrated in Figure 1b). The thermal energy of the electricity generation module (PV module and PETE module) can be given as:

$$\delta\dot{Q}_{\mathrm{diss}}(T_i) = \begin{cases} \delta E_{\mathrm{abs}}(T_i)\cdot\left(1-\eta_{T_i,\mathrm{PV}}\right), & \text{with PV module} \\ \delta E_{\mathrm{abs}}(T_i)\cdot\left(1-\eta_{T_i,\mathrm{PETE}}\right), & \text{with PETE module} \end{cases} \quad (11)$$

The convection loss and radiation loss of thermal energy are given as:

$$\delta\dot{Q}_{\mathrm{conv,loss}}(T_i) = h\cdot \mathrm{d}A\cdot(T_i - T_0) \quad (12)$$

$$\delta\dot{Q}_{\mathrm{rad,loss}}(T_i) = \varepsilon\cdot \mathrm{d}A\cdot\sigma\cdot(T_i^4 - {T_{\mathrm{sky}}}^4) \quad (13)$$

where ε is the emissivity of the absorber layer; h is the convective heat transfer coefficient (8 W m^{-2} K^{-1}); σ is Stefan-Boltzmann constant (5.67×10^{-8} W m^{-2} K^{-4})); A is the area of the photovoltaic/PETE module to receive solar energy; T_0 is the room temperature; T_{sky} is the sky temperature; T_i is the CO_2 temperature at the location of i along the CO_2 flow direction. The absorbed heat is the difference between the residual heat of PV/PETE module and the heat loss of the convection/radiation, expressed as:

$$\delta\dot{Q}(T_i) = \delta\dot{Q}_{\mathrm{diss}}(T_i) - \delta\dot{Q}_{\mathrm{conv,loss}}(T_i) - \delta\dot{Q}_{\mathrm{rad,loss}}(T_i) \quad (14)$$

In each controlled volume, an energy conservation equation will be solved to the temperature. Some assumptions have been reasonably made for analyze this system [12]: a) the flow resistance of CO_2 is neglected; b) the specific heat of PV/PETE modules is not taken into account. The key parameters for simulation of PV/PETE modules and the preheater are listed in Table 1.

Table 1. Key parameters for PV/PETE modules and the heating section

Parameter	Symbol	Value
Irradiation intensity	I (W m^{-2})	1000
Concentrator optical efficiency	η_{opt}	0.765 [13]
Photovoltaic module emissivity	ε	0.3 [14]
Photovoltaic module efficiency	η_{mod}	0.9
Temperature difference between photovoltaic panel and CO_2 flow	ΔT (K)	10
Ambient wind speed	v_{wind} (m s^{-1})	4
Ambient temperature	T_0 (K)	293
Convective heat transfer coefficient	h (W m^{-2} K^{-1})	8
Sky temperature	T_{sky} (K)	285 [15]
Length of heating section	L (m)	0.5
Width of heating section	W (m)	0.05
Height of heating section	H (m)	0.01

2.3 Mathematical model for electrolysis process

The external voltage required for electrolysis can be expressed as [16]:

$$V = E + \eta_{\mathrm{conc,c}} + \eta_{\mathrm{conc,a}} + \eta_{\mathrm{act,c}} + \eta_{\mathrm{act,a}} + \eta_{\mathrm{ohmic}} \quad (15)$$

where E is the equilibrium voltage; $\eta_{\mathrm{conc,c}}$ and $\eta_{\mathrm{conc,a}}$ are the concentration overpotentials of the cathode and anode, respectively; $\eta_{\mathrm{act,c}}$ and $\eta_{\mathrm{act,a}}$ are the activation overpotentials of the cathode and anode, respectively; and η_{ohmic} is the ohmic overvoltage. The following part describes the algorithm of each potential.

The equilibrium electrode potential is fitted as a function of temperature T using the data in the HSC software [17], given as:

$$E = 1.34397 - 4.46802\times10^{-4}T - 4.76241\times10^{-8}T^2 + 9.07576\times10^{-11}T^3 - 7.14257\times10^{-14}T^4 + 2.21046\times10^{-17}T^5 \quad (16)$$

The concentration overpotential of SOSE is caused by the resistance to the transport of reactant species arriving at the reaction site and product species flowing away the reaction site. The cathode concentration overpotential and anode concentration overpotential can be expressed as [18]:

$$\eta_{\text{conc,c}} = \frac{RT}{2F}\ln\left(\frac{(1+(JRTd_{\text{c}}/2FD^{\text{eff}}_{\text{CO}_2}p^{\text{In}}_{\text{CO}})}{1-(JRTd_{\text{c}}/2FD^{\text{eff}}_{\text{CO}_2}p^{\text{In}}_{\text{CO}})}\right) \quad (17)$$

$$\eta_{\text{conc,a}} = \frac{RT}{4F}\ln\left(\frac{\sqrt{(p^{\text{In}}_{\text{O}_2})^2+(JRT\mu d_{\text{a}}/2FB_g)}}{p^{\text{In}}_{\text{O}_2}}\right) \quad (18)$$

where J is the current density, and F is the Faraday constant; R is the ideal gas constant, d_{a} and d_{c} are the thickness of anode and cathode, respectively; $p^{\text{In}}_{\text{CO}}$ and $p^{\text{In}}_{\text{CO}_2}$ are the partial pressures of CO_2 and CO at the electrode surface; $D^{\text{eff}}_{\text{CO}_2}$ is the effective diffusion coefficient of CO_2; μ is the O_2 viscosity; B_{g} is the permeability. The anode concentration overpotential could be negligible in the calculation because the reactant O^{2-} ions are fully reacted at the anode-electrolyte interface without further diffusion into the porous anode [16]. Actually, Both the anode and cathode concentration overpotential are small enough with the current density J < 10000 A m^{-2} [18]. To briefly analyze this system, the concentration overpotentials are ignored due to the low current density (< 10000 A m^{-2}) in this research, and the simulation results are verified by comparing with the experimental results of Zhang *et al.* [19] (discussed in Section 3.1), which shows good agreements.

Activation overvoltage is related to the electrode kinetics at the reaction site. The relationship between electrode activation overvoltage and current density can be expressed by the classical Butler-Volmer equation [16]:

$$J = J_{\text{o},i}\left[\exp\left(\frac{\alpha zF\eta_{\text{act},i}}{RT}\right)-\exp\left(-\frac{(1-\alpha)zF\eta_{\text{act},i}}{RT}\right)\right],\ i=\text{a,c} \quad (19)$$

where $J_{0,i}$ is the exchange current density, and subscripts i=a, c represent the anode and cathode, respectively; α is the symmetry factor or the charge transfer coefficient; z is the number of electrons produced per reaction; and $\eta_{\text{act},i}$ is the activation overpotential. Therefore, the electrode activation overpotential can be expressed as:

$$\eta_{\text{act},i} = \frac{RT}{F}\ln\left[\frac{J}{2J_{0,i}}+\sqrt{\left(\frac{J}{2J_{0,i}}\right)^2+1}\right],\ i=\text{a,c} \quad (20)$$

At the cathode, the main electrochemical steps include CO_2 absorption, charge transport, CO desorption, and electrolyte absorption of oxygen ions. At the anode, the main electrochemical steps are charge transport and O_2 desorption. The above steps depend not only on operating parameters such as temperature, reactant concentration, etc., but also on material parameters, such as the three-phase boundary lengths. Studies have shown that the concentrations of reactants have little effect on the exchange current density, and the effect of temperature is more pronounced [20]. In summary, the exchange current density can be expressed as:

$$J_{0,\text{a}} = \gamma_{\text{a}}\exp\left(-\frac{E_{\text{act,a}}}{RT}\right) \quad (21)$$

$$J_{0,\text{c}} = \gamma_{\text{c}}\exp\left(-\frac{E_{\text{act,c}}}{RT}\right) \quad (22)$$

where γ_{a} and γ_{c} are the pre-exponential factors of the anode and cathode, respectively; $E_{\text{act,a}}$ and $E_{\text{act,c}}$ are the activation energy levels of the anode and cathode, which are found to be 1.2×10^5 J mol^{-1} [20] and 1.0×10^5 J mol^{-1} [21], respectively. It is recommended that the values of $J_{0,\text{a}}$ and $J_{0,\text{c}}$ are 2000 and 5000 A m^{-2} at a temperature of 1073 K [22], respectively. All of the key parameters for electrolysis section have been listed as Table 2.

According to Ohm's law, the ohmic overvoltage can be expressed as [16]:

$$\eta_{\text{ohmic}} = 2.99\times10^{-5}\cdot J\cdot L_{\text{e}}\cdot\exp\left(\frac{10300}{T}\right) \quad (23)$$

where L_{e} is the thickness (m) of the electrolyte.

This study calculates the one-dimensional steady state condition. Firstly, the temperature of each control volume of the heating section is solved, and then the total electricity production W_{PV} + W_{PETE} and the outlet steam temperature are calculated. The parameters related to the temperature of the electrolytic cell are calculated according to the CO_2 outlet temperature, and the voltage of each part and the total external voltage required V of the electrolytic cell are then obtained.

$$W_{\text{tot}} = W_{\text{PV}} + W_{\text{PETE}} = VJ \quad (24)$$

where W_{tot} is the total electricity generated from solar energy in both PV module and PETE module. According to the Equation 24, the current density of the electrolytic cell J could be calculated, and the amount of CO generated could be obtained accordingly.

$$n_{CO} = \frac{J}{2F} \quad (25)$$

Table 2. Key parameters for electrolysis section

Parameter	Symbol	Value
Electrolyte thickness	$l_{electrolyte}$ (μm)	500
Symmetry factor or the charge transfer coefficient	α	0.5
Number of electrons produced per reaction	z	2
Anode thickness	l_{anode} (μm)	100
Cathode thickness	$l_{cathode}$ (μm)	100
Anode activation energy	$E_{act,a}$ (J mol^{-1})	1.2 × 10^5 [20]
Cathode activation energy	$E_{act,c}$ (J mol^{-1})	1.0 × 10^5 [21]
Anode exchange current density	$J_{0,a}$ (A m^{-2})	2000 [22]
Cathode exchange current density	$J_{0,c}$ (A m^{-2})	5000 [22]

2.4 Thermodynamic evaluation

The first-law thermodynamic efficiency (energy efficiency), the second-law thermodynamic efficiency (exergy efficiency) and solar-to-fuel efficiency, are selected as three key gauges for the proposed system assessment. The energy efficiency focuses on the total amount of energy conversion during the reaction in this system, which is defined as:

$$\eta_{en} = \frac{\dot{n}_{CO} \cdot HHV_{CO} + \dot{Q}_{CO_2}}{I \cdot C \cdot A} \quad (26)$$

where $\dot{n}_{CO}$ is the flow rate of CO generation; HHV_{CO} is the higher heating value of CO (283 kJ mol^{-1}); C is the concentration level of sunlight; A is the area of the photovoltaic module to receive solar energy; $\dot{Q}_{CO_2}$ is the thermal power of CO_2 steam output from the SOEC electrolyzer, which equals to the thermal energy heating CO_2 from room temperature to the electrolyzing temperature. The denominator of Equation 26 is the total energy input, which is just the solar energy, and the numerator is the total energy generated, containing chemical energy of CO and thermal energy of the CO_2 unreacted (the thermal energy of CO and oxygen are limited and ignored in the calculation).

The exergy efficiency of the system is calculated for assessment of the energy quality utilization, given as:

$$\eta_{ex} = \frac{\dot{n}_{CO} \cdot Ex_{CO} + \dot{Q}_{CO_2} \cdot (1 - \frac{T_0}{T_H})}{\dot{E}x_{solar}} \quad (27)$$

where T_H is the temperature of CO_2 in electrolyzer; the exergy of CO, Ex_{CO}, is taken as 275 kJ mol^{-1} [23], and the exergy input of solar energy is explicitly expressed as [24]:

$$\dot{E}x_{solar} = [1 - \frac{4T_0}{3T_{sun}} + \frac{1}{3}(\frac{T_0}{T_{sun}})^4] \cdot (I \cdot C \cdot A) \quad (28)$$

where T_{sun} is the temperature of the sun surface, taken as 5800 K. Equation 27 exhibits the ratio of exergy of products to the total exergy of solar energy input to the system. The solar-to-fuel efficiency is defined as the ratio of higher heating value of CO generated to the solar energy input, shown as:

$$\eta_{s \to f} = \frac{\dot{n}_{CO} \cdot HHV_{CO}}{I \cdot C \cdot A} \quad (29)$$

3. RESULTS AND DISCUSSIONS

3.1 SOEC verification

To verify the accuracy of the simulation of SOEC, a comparison between this research to the results from experiment [19, 25-27] is given in Figure 4, which shows a quite close results (relative error < 7.5%) and verifies the solid of this simulation results.

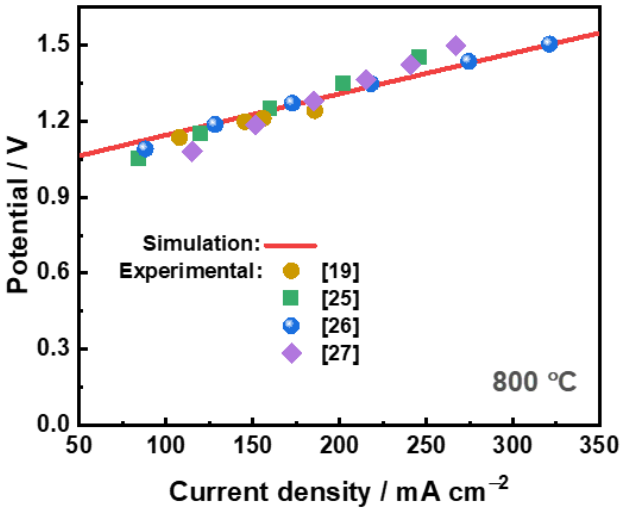

Figure 4. Verification of the present simulation results with experimental data [19, 25-27] of SOEC for CO_2 electrolysis.

3.2 Performance of PV cells, PETE, and preheater

The outlet temperature of CO_2 flow and solar-to-electricity efficiency versus different flow rate of CO_2 at room temperature is exhibited in Figure 5. The concentration ratio *C* is set at 60, which falls into the typical range of commercial line-focused solar collector (30-70), unless stated otherwise.

As the flow rate of CO_2 increases from standard 1 L min^{-1} to 100 L min^{-1}, more thermal energy will be taken away and the temperature will increase slowly (Figure 5a). Thus, the outlet temperature can be controlled and manipulated by change the flow rate of CO_2 inlet.

As the solar-to-electricity efficiency is functions of temperature (Equations 9 and 10), it also varies with the flow rate changing, which is given in Figure 5b. It is clear that the CO_2 feeding decreases the decline rate of PV efficiency, which is from 31.9% (20 °C) to 23% (250 °C).

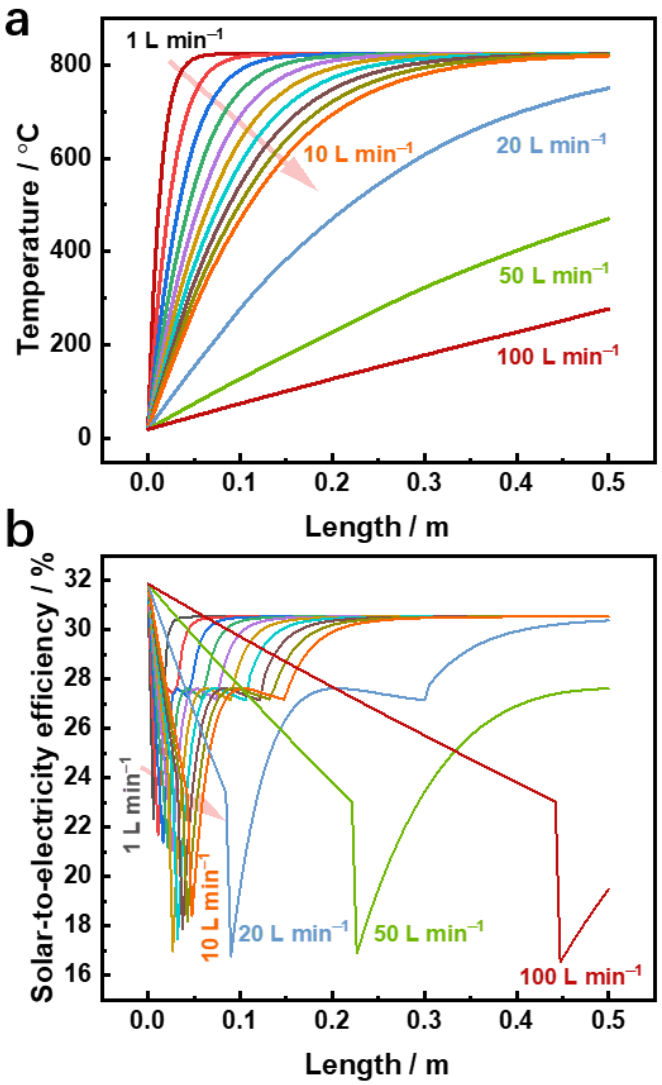

Figure 5. The CO_2 temperature (a) and solar-to-electricity of PV or PETE (b) variation with different standard flow rate of CO_2 along the length direction.

The solar energy is unstable in the daytime, and the irradiation power is also variable. To analyze the performance of this system under different input solar power, the concentration is assumed to be changed from 10 to 80, and thus the power of solar irradiation input is from 10 kW m^{-2} to 80 kW m^{-2}, given in Figure 6.

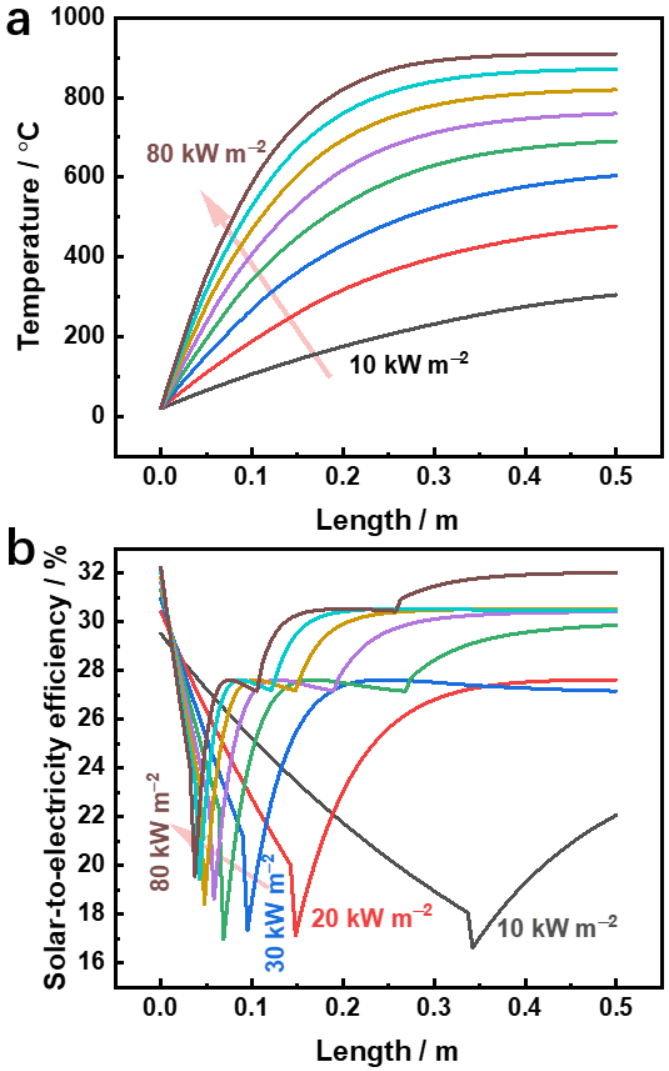

Figure 6. The CO_2 temperature (a) and solar-to-electricity of PV or PETE (b) variation with different solar irradiation power input along the length direction under a CO_2 flow rate of 10 L min^{-1}.

With the increase of power input, the CO_2 temperature under stable condition rises up, and the related solar-to-electricity efficiency also changes. The start value of the solar-to-electricity also varies even all of them at a certain room temperature (20 °C in this research), which results from the influence of variation of concentration on PV cell efficiency (Equation 9).

The influence of power input on the outlet temperature could be limited by the proactive control of flow rate of CO_2. For example, if the irradiation decreases, the influence can be reduced by the decline of CO_2 flow rate, leading to a relative stable temperature and solar-to-electricity efficiency.

3.3 Efficiency of the system

The energy efficiency, exergy efficiency, solar-to-fuel efficiency, and average solar-to-electricity efficiency are calculated and given in Figure 7. As the outlet temperature decreases with the enhancement of flow rate and the decline of solar irradiation input (Figure 8), more heat loss (heat convection and radiation in Equations 12 and 13) occurs, and thus results in a low energy efficiency (red line in Figure 7).

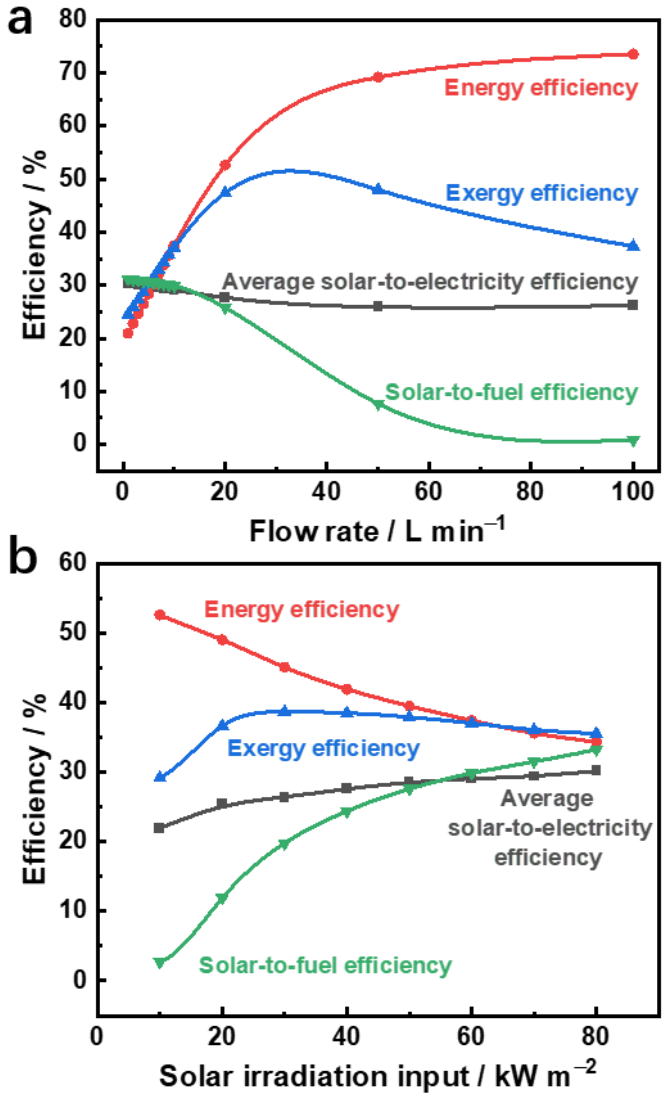

Figure 7. Thermodynamic efficiencies of the system variation with (a) flow rate of CO_2 and (b) solar irradiation input. The solar irradiation in a and CO_2 flow rate in b are 60 kW m^{-2} and 10 L min^{-1}.

The exergy efficiency (blue line) has a peak in both Figure 7a and b. In a relative low flow rate range (< 20 L min^{-1}), the variation of outlet temperature is not obvious (Figure 8a), and the ratio of thermal exergy contained in thermal energy is almost constant. Thus, a high flow rate contains more sensible heat, increasing the exergy efficiency. When the flow rate of CO_2 is quite high (> 30 L min^{-1}), the outlet temperature decreases a lot, resulting in low thermal exergy and low exergy efficiency.

With the solar irradiation input increases, the outlet temperature increases with a low slope (Figure 8b), and

the thermal exergy increases, resulting in a high exergy efficiency at an irradiation input of around 25 kW m^{-2}. With the irradiation further increasing, more heat loss limits the enhancement of exergy and decrease it slowly.

The solar-to-fuel efficiency has a similar trend to average solar-to-electricity efficiency as the fuel (CO) is generated from the electricity generated. The average solar-to-electricity efficiency is calculated from the ratio of all the electricity generated to the total solar energy input to PV cells and the PETE module, which decreases slowly with the flow rate increasing, mainly because the electricity generated ratio from PETE decreases (Figure 5b), which has a relatively stable and high solar-to-electricity efficiency.

With the increase of solar irradiation, both the solar-to-electricity efficiency of PV and PETE are increased (Equations 9 and 10, Figure 6b), and the electricity generation ratio from PETE also enlarges, leading to high average solar-to-electricity efficiency and solar-to-fuel efficiency. The energy efficiency, exergy efficiency, and solar-to-fuel efficiency can reach 73.5%, 48.0%, and 33.3%, respectively, in this proposed solar-driven system.

The CO_2 conversion in Figure 8 is defined as molar ratio of the amount of CO_2 that can be converted in SOEC to the amount of CO_2 feeding at room temperature. The conversion > 100% indicates that SOEC can convert more CO_2 than that feeding inside. As the flow rate of CO_2 increases, the CO_2 conversion reduces due to the increment of denominator (feeding amount). With the increase of solar irradiation input, more electricity can be generated (Figure 7b), and thus larger amount of CO_2 can be converted at a certain feeding amount (10 L min^{-1}), leading to a high CO_2 conversion.

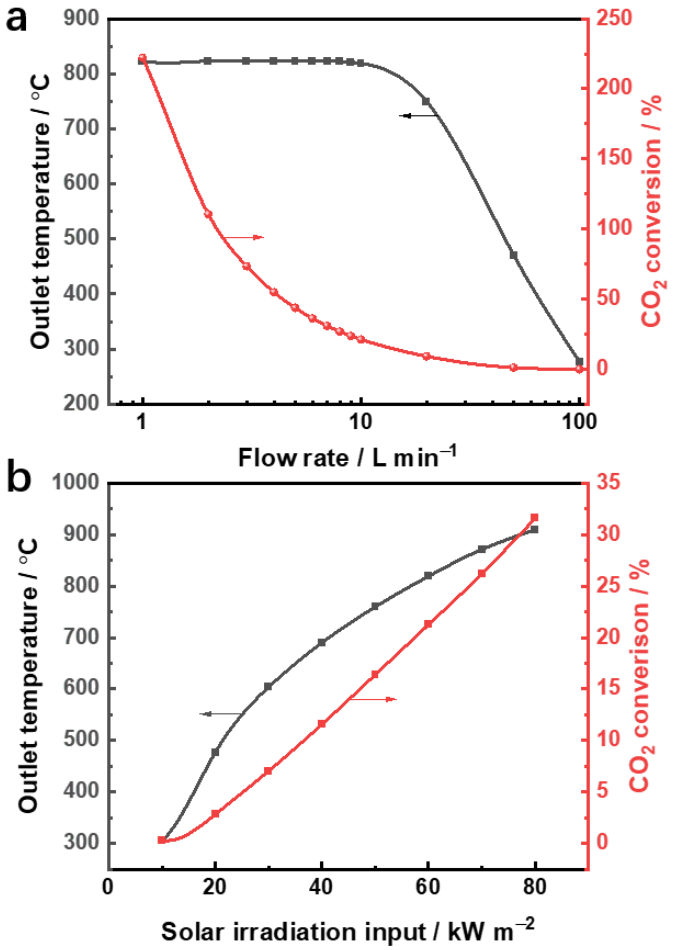

Figure 8. Outlet temperature of CO_2 and CO_2 conversion versus (a) flow rate of CO_2 and (b) solar irradiation input.

4. CONCLUSIONS

In this research, a novel solar-driven CO_2 splitting system is proposed, which contains PV cells, PETE, and SOEC, and it can efficiently utilize the full spectrum of solar energy in a wide temperature range in cascade. The solar energy can be converted into electricity with high energy level efficiently due to the cooling effect of CO_2 fluid first, and then the heated CO_2 was fed into SOEC for electrolysis with a low Gibbs free energy requirement owing to the high-temperature CO_2 heated by residual heat from PV cells and PETE module.

More thermal energy with relatively low energy level can be converted into chemical energy in this system compared to that of H_2O splitting, resulting in a high-efficient storage and conversion of solar thermal energy and solar power. The energy efficiency, exergy efficiency, and solar-to-fuel efficiency can reach 73.5%, 48.0%, and 33.3%, respectively. This study represents a step forward in rational design of a high-efficient solar CO_2 splitting system, and gives guidance to other solar fuel electrolysis systems.

ACKNOWLEDGEMENT

This work is funded by the National Natural Science Foundation of China (No. 51906179 and No. 52006124), the State Key Laboratory of Clean Energy Utilization (Project No. ZJUCEU2020015), the China Postdoctoral Science Foundation (No. 2019M660588) and the Beijing Institute of Technology Research Fund Program for Young Scholars (No. XSQD-202103005).

REFERENCE

[1] Kato N, Mizuno S, Shiozawa M, Nojiri N, Kawai Y, Fukumoto K, et al. A large-sized cell for solar-driven CO_2 conversion with a solar-to-formate conversion efficiency of 7.2%. Joule. 2021;5:687-705.

[2] Gong E, Ali S, Hiragond CB, Kim HS, Powar NS, Kim D, et al. Solar fuels: research and development strategies to accelerate photocatalytic CO_2 conversion into hydrocarbon fuels. Energy & Environmental Science. 2022;15:880-937.

[3] Zoller S, Koepf E, Nizamian D, Stephan M, Patané A, Haueter P, et al. A solar tower fuel plant for the thermochemical production of kerosene from H_2O and CO_2. Joule. 2022;6:1606-16.

[4] Chueh WC, Falter C, Abbott M, Scipio D, Furler P, Haile SM, et al. High-flux solar-driven thermochemical dissociation of CO_2 and H_2O using nonstoichiometric ceria. Science. 2010;330:1797-801.

[5] Tou M, Michalsky R, Steinfeld A. Solar-driven thermochemical splitting of CO_2 and in situ separation of CO and O_2 across a ceria redox membrane reactor. Joule. 2017;1:146-54.

[6] Li Y, Zhang L, Yu B, Zhu J, Wu C. CO_2 High-Temperature Electrolysis Technology Toward Carbon Neutralization in the Chemical Industry. Engineering. 2023;21:101-14.

[7] Wang H, Li W, Liu T, Liu X, Hu X. Thermodynamic analysis and optimization of photovoltaic/thermal hybrid hydrogen generation system based on complementary combination of photovoltaic cells and proton exchange membrane electrolyzer. Energy Conversion and Management. 2019;183:97-108.

[8] Iora P, Aguiar P, Adjiman C, Brandon NP. Comparison of two IT DIR-SOFC models: Impact of variable thermodynamic, physical, and flow properties. Steady-state and dynamic analysis. Chemical Engineering Science. 2005;60:2963-75.

[9] Kribus A, Mittelman G. Potential of polygeneration with solar thermal and photovoltaic systems. Journal of solar energy engineering. 2008;130.

[10] Green MA, Emery K, Hishikawa Y, Warta W, Dunlop ED. Solar cell efficiency tables (version 48). Progress in Photovoltaics: Research and Applications. 2016;24:905-13.

[11] Tang W. Based on the mechanism of photon-enhanced electron emission for solar energy converters: University of Chinese Academy of Sciences; 2014.

[12] Wang H, Kong H, Pu Z, Li Y, Hu X. Feasibility of high efficient solar hydrogen generation system integrating photovoltaic cell/photon-enhanced thermionic emission and high-temperature electrolysis cell. Energy Conversion and Management. 2020;210:112699.

[13] Zarza E, Rojas ME, González L, Caballero JM, Rueda F. INDITEP: The first pre-commercial DSG solar power plant. Solar Energy. 2006;80:1270-6.

[14] Li W, Hao Y. Explore the performance limit of a solar PV–thermochemical power generation system. Applied energy. 2017;206:843-50.

[15] Madival A, Jai KS, Sudeshkumar CA, Vishalreddy, Srinivas MR, Krupashankara MS. Studies on Effect of Varying Geometric Parameters of Solar Receiver Tube on Thermal Loss Suffered By It. 2015.

[16] Ni M, Leung MK, Leung DY. Parametric study of solid oxide steam electrolyzer for hydrogen production. International Journal of Hydrogen Energy. 2007;32:2305-13.

[17] Roine A. HSC Chemistry 5.11. Outokumpu Research Oy, Pori, Finland. 2002;76.

[18] Ni M, Leung MK, Leung DY. Energy and exergy analysis of hydrogen production by solid oxide steam electrolyzer plant. International journal of hydrogen energy. 2007;32:4648-60.

[19] Zhang L, Xu C, Sun W, Ren R, Yang X, Luo Y, et al. Constructing perovskite/alkaline-earth metal composite heterostructure by infiltration to revitalize CO_2 electrolysis. Separation and Purification Technology. 2022;298:121475.

[20] Costamagna P, Honegger K. Modeling of solid oxide heat exchanger integrated stacks and simulation at high fuel utilization. Journal of the Electrochemical Society. 1998;145:3995.

[21] Zhu H, Kee RJ. A general mathematical model for analyzing the performance of fuel-cell membrane-electrode assemblies. Journal of Power Sources. 2003;117:61-74.

[22] Chan S, Xia Z. Polarization effects in electrolyte/electrode-supported solid oxide fuel cells. Journal of Applied Electrochemistry. 2002;32:339-47.

[23] Wang H, Kong H, Wang J, Liu M, Su B, Lundin S-TB. Theoretical thermodynamic efficiency limit of isothermal solar fuel generation from H_2O/CO_2 splitting in membrane reactors. Molecules. 2021;26:7047.

[24] Wang B, Kong H, Wang H, Wang Y, Hu X. Kinetic and thermodynamic analyses of mid/low-temperature ammonia decomposition in solar-driven hydrogen permeation membrane reactor. International Journal of Hydrogen Energy. 2019;44:26874-87.

[25] Cao Z, Wei B, Miao J, Wang Z, Lü Z, Li W, et al. Efficient electrolysis of CO_2 in symmetrical solid oxide electrolysis cell with highly active $La_{0.3}Sr_{0.7}Fe_{0.7}Ti_{0.3}O_3$ electrode material. Electrochemistry Communications. 2016;69:80-3.

[26] Ye L, Hu X, Wang X, Chen F, Tang D, Dong D, et al. Enhanced CO_2 electrolysis with a $SrTiO_3$ cathode through a dual doping strategy. Journal of Materials Chemistry A. 2019;7:2764-72.

[27] Kulkarni AP, Giddey S, Badwal SPS. Efficient conversion of CO_2 in solid oxide electrolytic cells with Pd doped perovskite cathode on ceria nanofilm interlayer. Journal of CO_2 Utilization. 2017;17:180-7.